Eng. Sci., 2025, **38**, 1848

Engineered Science

DOI: https://dx.doi.org/10.30919/es1848

Active Transmission-type Polarization-modulated Metasurface by Tailoring Electromagnetic Wave Propagation Modes

Zhe Qin,[1,2] Yongfeng Li,[1,2,*] He Wang,[1,2] Zhibiao Zhu,[1,2] Lixin Jiang,[1,2] Wanwan Yang,[1,2] Hongya Chen,[1,2] Lin Zheng,[1,2] Jiafu Wang[1,2] and Hua Ma[1,2,*]

Abstract

Active reconfigurable metasurfaces provide unprecedented dynamic and real-time control of electromagnetic (EM) waves, which have attracted a great deal of attention. Despite significant progress, achieving dynamic polarization modulation with high transmission efficiency is still a challenging task. Here, we propose a paradigm that possesses the possibility of dynamically switching transmission modes between the waveguide and the spoof surface plasmon polariton (SSPP) for tailoring transmission waves. Combined with the dispersion engineering by changing the states of the voltage-driven positive-intrinsic-negative (PIN) diode, the phase difference of x- and y-components can be flexibly manipulated for achieving different polarization states in a wide frequency range. As a proof-of-concept, one of the unique states for obtaining circular polarization conversion with the Pancharatnam-Berry (PB) phase principle is selected for achieving a spin-orbital angular momentum dynamic converter. The experimental results agree well with the simulations, which verify the feasibility of the proposed strategy. Significantly, our work not only provides an alternative way to dynamically modulate the transmission polarization state but also has promising applications in holographic imaging, intelligent beam forming, and adaptive stealth.

Keywords: Polarization modulation; Reconfigurable metasurface; Waveguide mode; Spoof surface plasmon polariton mode; PIN diode; Angular momentum converter.

Received: 28 July 2025; Revised: 15 October 2025; Accepted: 28 October 2025.

Article type: Research article.

1. Introduction

Polarization, as one of the properties of electromagnetic (EM) waves, not only affects the propagation characteristics of EM waves but also directly relates to the quality of the signal, the capacity of the system, and the ability to recognize the target. It guarantees potential applications for wireless communication and detection systems. By exploiting orthogonal polarization states, systems can effectively double channel capacity without increasing bandwidth or power. Moreover, polarization agility helps mitigate polarization mismatch losses in mobile scenarios, reduces interference, and enhances signal security. From 5G communication to the future 6G communication, satellite communication, Internet of Things, and polarization technology will become the key to enhancing system performance. Therefore, the explorations of efficiently regulating the polarization of EM waves have emerged, which is not only of great theoretical significance but also will have a profound impact on the development of engineering applications.

Metasurfaces, consisting of elaborated meta-atoms in a deep sub-wavelength scale, have attracted a great deal of attention in various applications. Owing to the unique properties that are unavailable in natural media, metasurfaces can be applied to achieve a lot of extraordinary physical phenomena, such as negative refractions,[1,2] anomalous reflections,[3,4] and integrated radiation-scattering characteristics.[5] Besides, they have exhibited outstanding and tailorable capabilities in modulating EM waves, facilitating plenty of devices and applications, including invisibility cloaks,[6-9] holography,[10-12] orbital angular momentum (OAM) generations,[13-17] and so on. In particular, metasurface-based polarization converters have the advantages of small size, easy integration, low loss, and low energy consumption compared with conventional birefringent crystal-based or ferrite variable polarizers. Over the past decade, researchers have

---

[1] *Department of Basic Science, Air Force Engineering University, Xi'an, 710051, China*

[2] *Shaanxi Key Laboratory of Artificially-Structured Functional Materials and Devices, Xi'an, Shaanxi, 710051, China*

**Email:* liyf217130@126.com (Y. Li); mahuar@163.com (H. Ma)

successively realized various forms of polarization-modulated metasurfaces, including linear-to-linear (LTL),[18-20] linear-to-circular (LTC),[21-24] and circular-to-circular (CTC).[25,26]

Early polarization-modulated metasurfaces are mainly passive, and once designed and finalized, their ability to modulate the polarization of EM waves is fixed, which fails to meet the growing demand for real-time and intelligent control in modern devices. Therefore, the active metasurfaces for dynamically controlling EM waves are highly desired. The emerging active metasurfaces typically resort to extra active elements, such as electronically controlled components,[27-29] phase change materials,[30,31] graphene,[32,33] and mechanically tunable materials.[34,35] Especially, tuning mechanisms based on electronically controlled components such as varactor diodes, PIN diodes, and varistor diodes have attracted more attention in the microwave region because of their faster response and higher level of integration. However, most of the existing active polarization-modulated metasurfaces can hardly prevent the framework of reflection-type, thus the effective strategies for modulating transmitted waves are still insufficient. To date, a common issue with most active transmission-type metasurfaces is the limitation of the feeder network for transmitted functions. In the realm of this academic challenge, various attempts to achieve active transmission-type polarization-modulated metasurfaces have emerged. In 2014, Luo *et al*. proposed an active chiral metasurface, which switches its polarization not only between chirality and isotropic but also between left-handed and right-handed chirality by controlling the loaded PIN diodes in each meta-atom.[36] In 2019, a polarization rotator based on the active metasurface that can dynamically tune the polarization of an incident wave in transmission and achieve a remarkable total rotation angle range of 146° was proposed by Wu *et al*.[37] In addition, quite a few tunable metasurfaces based on resonator structures have been explored.[38-40] Although these efforts possess the advantages of real-time reconfigurability and fast response, they still have the drawbacks of either low transmission efficiency or limited tunable range. Fortunately, the strategy based on the spoof surface plasmon polariton (SSPP) provides an alternative option to overcome this academic difficulty.[22] The realization of dynamically switching propagation modes is expected to provide another route for efficient transmission polarization modulation.

Here, we propose a dynamic polarization modulation mechanism based on phase control implemented by switching the propagation modes between the SSPP and the waveguide. By changing the states of the PIN diode, active control of the transmission phase can be achieved with high transmission efficiency to tailor the polarization state of the transmitted wave. As a proof-of-concept, a spin-to-orbital angular momentum dynamic converter with quasi-continuous spatial phase response based on the PB phase generated by the circular polarization conversion is implemented. By properly arranging the preset meta-atoms along an Archimedean spiral, the rotated phase distribution covering 0 to 4π is achieved. The states of the PIN diodes are controlled via a field programmable gate array (FPGA), which enables the programming of the polarization of the EM wave. By dynamically tailoring the polarization, dynamic switching of circularly polarized wave-carrying spin angular momentum (SAM) and vortices with the topological charge of $l = \pm 2$ can be acquired.

2. Experimental

The schematic diagram of the proposed active transmission-type polarization-modulated metasurface is illustrated in Fig. 1. By changing the states of the PIN diodes, dynamic switching of the transmission mode between the SSPP and waveguide mode is achieved to obtain a tailorable transmission phase. The OAM is generated based on quasi-continuous phase gradients under the incidence of a circularly polarized wave-carrying SAM.

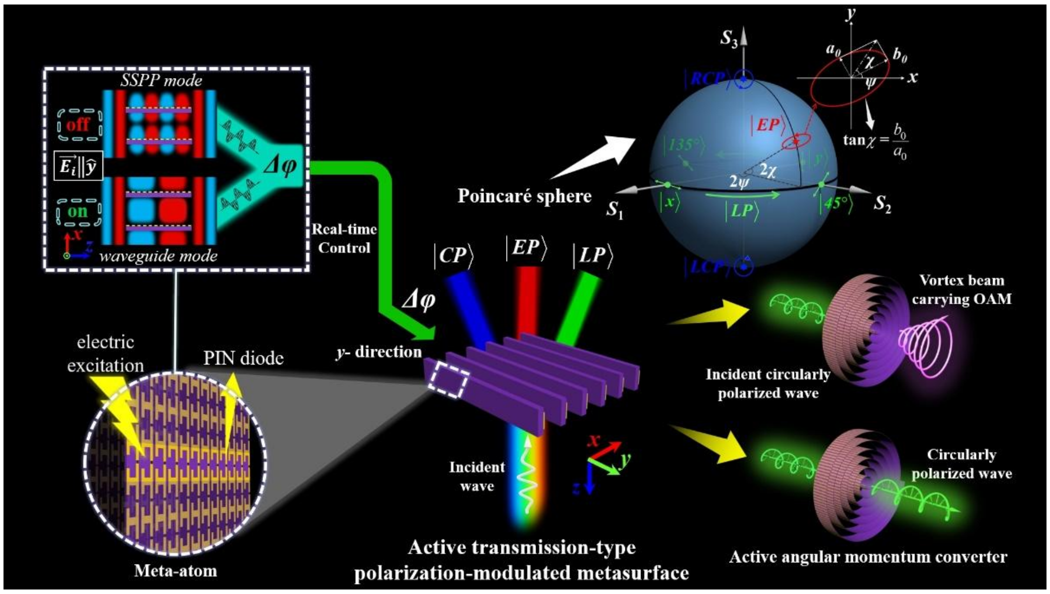

Fig. 1: The schematic diagram of the proposed active transmission-type polarization-modulated metasurface.

As shown in Fig. 2a, the meta-atom consists of split square rings arranged periodically along the *x*-direction, with the length *a* and the width *b*, which is printed on one side of the dielectric substrate with the thickness *h*. There is a gap in the middle of the long strip of the square ring, and a PIN diode is welded across the gap. When inactivated, the PIN diode operates as an open circuit or a small capacitor. In this case, the long strip splits at the gap, and the metal structure resembles a plasmonic structure. When the *y*-polarized EM wave is incident, it can be efficiently coupled into the split square ring. The wave propagates through the metallic structure in the SSPP mode, and the corresponding propagation constant $k_{z\text{-}SSPP}$ is large and can be expressed as Eq. (1):

$$k_{z-SSPP} = k_0\sqrt{1+\frac{t^2}{b^2}\tan^2\left[k_0(a-2e)\right]} \tag{1}$$

where *e* is the width of the metal line, and *t* is the distance between the metal lines of the split square rings, as shown in Fig. 2a. $k_{z\text{-}SSPP}$ is proportional to the square ring widths *a*. For verification, we simulate the dispersions with different square ring widths *a* = 5, 6, and 7 mm, by the computer simulation technology (CST) Microwave Studio, and the simulation results are illustrated in Fig. 2b, where the red line represents free-space waves. The simulation curves correspond to the SSPP mode, where the wave-vector component k_z is smaller than the wave-vector of the free-space wave k_0 and decreases as the length *a* increases. Moreover, the asymptotic frequency moves to a lower frequency as *a* increases. When the frequency exceeds the asymptotic frequency, the SSPP mode will be cut off, and the transmission waves will be suppressed. Furthermore, the corresponding transmission amplitudes under the *y*-polarized wave incident are simulated, and the simulation results with different square ring widths are demonstrated in Fig. 2c. The transmission amplitude dramatically declines above frequencies *f* = 11.7, 13.3, and 13.8 GHz, and the transmission waves are suppressed, which is consistent with the asymptotic frequencies. Therefore, the wave propagates through the metallic structure in the SSPP mode.

On the contrary, when the power intensity reaches a specified threshold and the PIN diode is activated, it operates as a short circuit or small resistor. The long strip is connected, and the metal structure resembles a metal plate in the *y* direction. At this point, the *y*-polarized wave propagates in the array in the waveguide mode, and the corresponding propagation constant $k_{z\text{-}wg}$ is small and can be expressed as Eq. (2):

$$k_{z-wg} = \sqrt{k_0^2-\left(\frac{i\pi}{n_0 g+h}\right)^2}, \left(i\in N^+\right) \tag{2}$$

where *g* is the distance between the dielectrics, n_0 is the refractive index of the medium, and *i* is a positive integer. The simulated dispersions of *y*-polarized waves with different dielectric thicknesses *h* = 0.5, 2, and 3.5 mm are shown in Fig. 2b. The wave-vector component k_z is less than k_0 and increases as *h* increases. Also, the cut-off frequency moves to a higher frequency as *h* increases. In addition, the simulation results of the transmission amplitude under the *y*-polarized wave incident are shown in Fig. 2d. The transmission amplitudes are high, and the waves exhibit efficient transmission at frequencies above 7.1, 7.7, and 8.3 GHz, which mainly correspond to the cut-off frequencies of the waveguide mode. In this case, the wave propagates through the metallic structure in the waveguide mode, corresponding to the mode number *i* = 1.

To study the working mechanism, the surface current distributions of the metal structure under the incidence of the *y*-polarized wave along the +*z* direction are observed, and the simulation results at 10.0 GHz are shown in Fig. 2e. When the PIN diode is inactivated, the split square ring works as a magnetic dipole, inducing the surface current to flow in the loop. In contrast, when the PIN diode is activated, the main surface current flows along the direction of the incident polarized electric field, and the split square ring is like an electric-inductive-capacitive (electric-LC) resonator and works as an electric dipole. Consequently, the optimization of the geometry of the split square ring, such as length *a* and width *b*, enables the adjustment of the surface resistance and magnetic impedance to achieve the tailoring of the transmission coefficient. Besides, the electric field distributions at 10.0 GHz are simulated to visualize the propagation of waves in the SSPP and waveguide modes, and the distributions of the electric field *y* component in the *xoz*-plane are illustrated in Fig. 2f. When the PIN diode is “off”, the incident electric field *y* component is coupled to and confined entirely near the square split rings, and the wave propagates in the SSPP mode with a small wavelength. However, when the PIN diode is “on”, the incident electric field *y* component is coupled into the waveguide with a large wavelength.

Switching of modes between the waveguide and SSPP can be realized by simply changing the state of the PIN diode. Because of the nonlinear dispersion relationship between these two modes, the transmission phase difference $\Delta\varphi$ can be tailored in a wide frequency band by designing the dispersion. The wave-vector component $k_{z\text{-}SSPP}$ in the SSPP mode is larger than the wave-vector component $k_{z\text{-}wg}$ in the waveguide mode, which means that the phase of the SSPP mode is always advanced over the waveguide. Therefore, $\Delta\varphi$ can be expressed as Eq. (3):

$$\Delta\varphi = \left(\sum k_{z-SSPP} - k_{z-\mathrm{wg}}\right)b \tag{3}$$

By optimizing the geometry of the meta-atom, such as *a*, *g*, and *h*, the waveguide mode and the SSPP mode can operate in the same frequency band. A desired transmission phase difference can be achieved by changing the state of the PIN diode. A higher phase shift can be achieved by increasing the number of split square rings along the *z* direction, and the accumulated phase difference is $\Phi = n_{on}\times\Delta\varphi$, where n_{on} is the

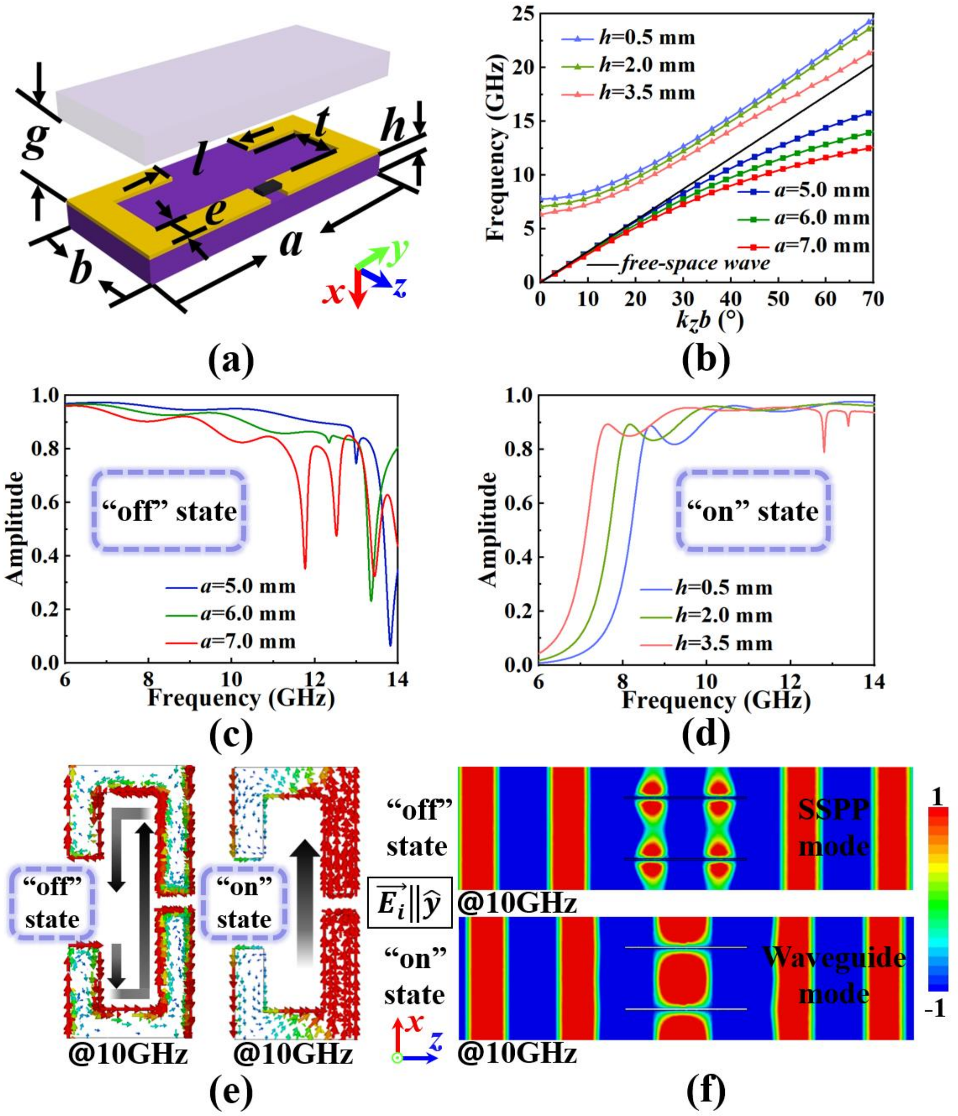

Fig. 2: a) The topology of the proposed meta-atom. b) Dispersion diagrams of the y-polarized wave with different dielectric thicknesses h and square ring widths a. c) and d) The corresponding simulated transmission amplitudes with different square ring widths a and dielectric thicknesses h, respectively. e) The simulated surface current distribution along the metallic split-ring at 10.0 GHz. f) The electric field distributions in the xoz-plane at 10.0 GHz.

number of PIN diodes in the "on" state.

As a validation, we select a design with a phase shift step of 30° from the simulation results and the meta-atom consists of twelve resonant rings to cover 360° transmission phase shift, as shown in Fig. 3a. The dispersion curves of the waveguide mode and SSPP mode are shown in Fig. 3b. The dispersion phase difference between these two modes is exactly 30° in the frequency band of 8.1-13.2 GHz. The split square ring metal patches with optimized length a = 6 mm and width b = 2.5 mm are etched on one side of the F4B dielectric substrate of optimized thickness h = 0.5 mm with dielectric constant ε_r = 2.65 and loss tangent tan δ = 0.001. Different rings on a meta-atom are connected in parallel, and the PIN diodes can be in different states. Each ring is connected in series with the rings along the y-direction, which ensures that the PIN diodes on a series circuit are in the same state. The states of different numbers n_{on} of PIN diodes in the "on" state vary from 0 to 12 are shown in Fig. 3c. To realize the goal of dynamic control, we use the BAP70-02 diode from NXP Semiconductors, which has the advantage of low diode capacitance and series inductance. According to the datasheet,[41] the forward voltage of the PIN diode is +1.1 V, and the response time is approximately 1.25 ns, which is sufficient for the intended application. The equivalent circuit of the PIN diode is a lumped resistor-inductor-capacitor (RLC) series circuit with the parasitic capacitance C_s= 0.25 pF, the parasitic inductance L_s = 0.6 nH, the variable resistance R_{ON} = 4.2 Ω, and R_{OFF} = 50000 Ω. Besides, the other optimized geometric parameters are as follows: t = 1.3 mm, g = 18 mm, c = 36.6 mm, l = 2 mm, e = 0.6 mm, and s = 0.6 mm.

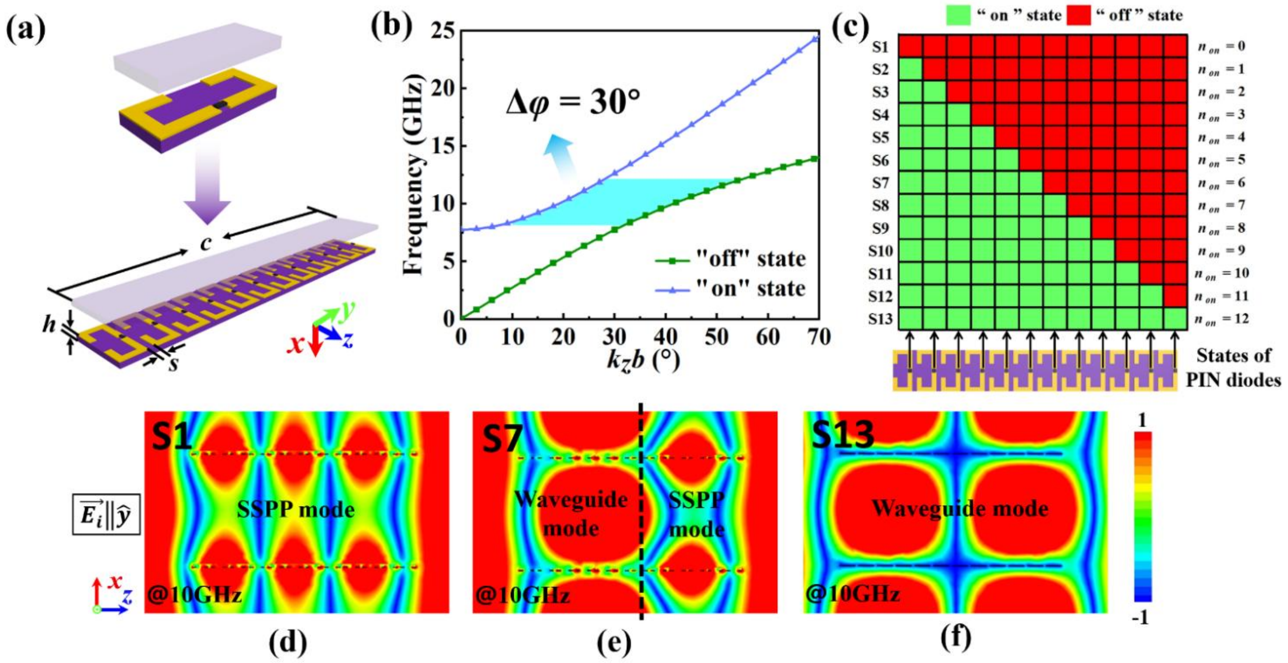

Fig. 3: a) The topology of the meta-atom, which consists of twelve resonant rings. b) The dispersion diagrams of the design with a phase shift step of 30°. c) The states of different numbers n_{on} of PIN diodes in the "on" state vary from 0 to 12. d-f) The electric field distributions in the xoz-plane at 10.0 GHz when the PIN diodes are in S1, S7, and S13, respectively.

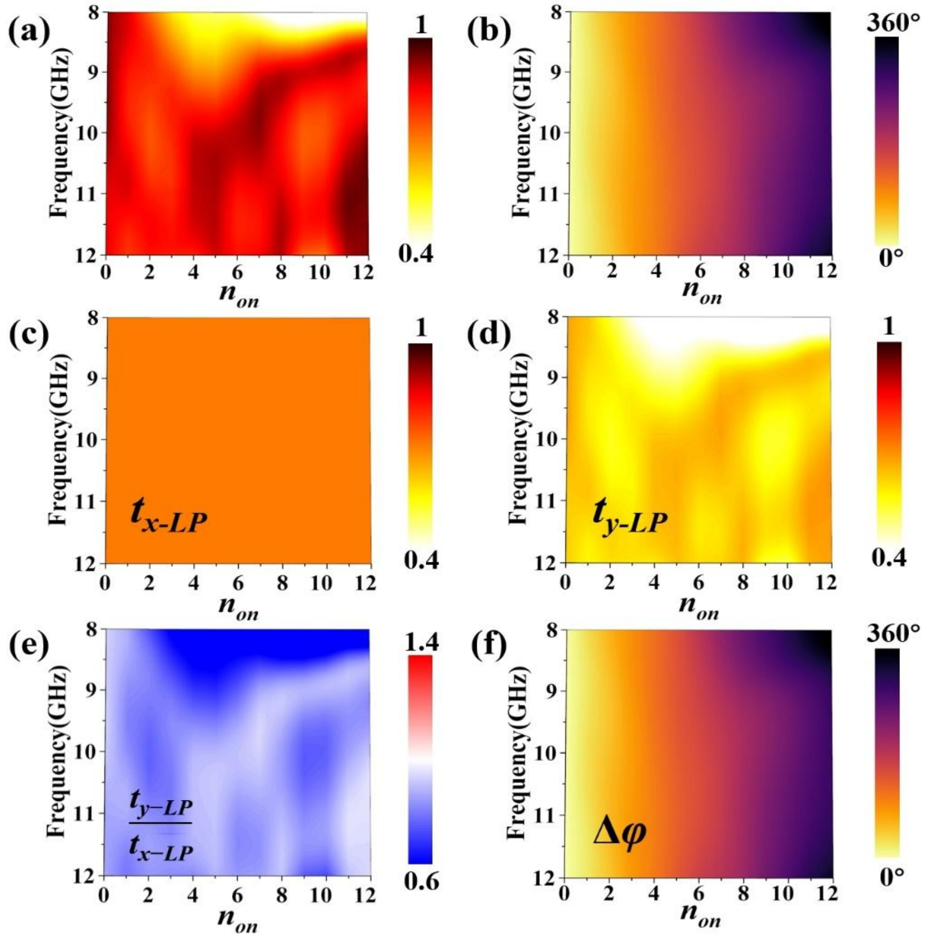

Fig. 4: a-b) The transmission amplitude and phase response with the different number of PIN diodes in the "on" state under *y*-polarized wave incidence, respectively. c-d) The *x*- and *y*-polarized transmission amplitude in different states of PIN diodes under LP wave incidence, respectively. e) The proportionality of $t_{x\text{-}LP}$ and $t_{y\text{-}LP}$ in different states of PIN diodes. f) The phase difference between the *x*- and *y*-polarized transmitted wave.

Under y-polarized wave incidence, the transmission phase and amplitude of different states of the PIN diodes are simulated as shown in Figs. 4a-b, respectively. It is worth noting that the horizontal axis represents discrete integer values of non. To visually illustrate the trend of phase/amplitude variation with frequency under different states, the plots are provided for visual guidance only. In the frequency band of 9.3-11.9 GHz, the transmission amplitudes all exceed 0.75. In addition, when n_{on} is varied from 0 to 12, the phases of the corresponding transmission waves in the frequency band of 9.1-12.1 GHz are approximately 0, 30°, 60°, 90°, 120°, 150°, 180°, 210°, 240°, 270°, 300°, 330°, and 360°, respectively. In fact, wave propagation is not strictly limited to a binary switch between waveguide or SSPP modes. Instead, the meta-atom array allows hybrid mode propagation depending on the spatial distribution of states of the PIN diodes. The electric field distributions on the xoz-plane at 10.0 GHz are shown in Figs. 3d-f for different states of the diode. In S1, waves propagate primarily in the SSPP mode. In S7, waves propagate in waveguide mode in the first half and SSPP mode in the latter half. In S13, waves propagate primarily in the waveguide mode. The results show that due to the subwavelength scale of the meta-atoms and the gradual phase accumulation along the propagation direction, the two modes can achieve relatively efficient coupling at the interface. The proposed metasurface realizes arbitrary control of the transmission phase for y-polarized waves, but has a negligible influence for x-polarized waves, so that we can use the transmission phase difference between x- and y-polarized to synthesize various polarization states. The polarization space (Poincaré sphere) can intuitively visualize the polarization states of light and the evolution of polarization between the different states, as illustrated in Fig. 1. An arbitrary fully polarized state can be represented by a point on the surface of the sphere, while a partially polarized state can be represented by a point inside the sphere. Since any point on the sphere surface can be represented by its latitude and longitude, correspondingly, any fully polarized state in the polarization space can be represented by the ellipticity angle χ and the orientation angle ψ, which describe the shape of the ellipse and the direction of the principal axis of the ellipse, respectively.

The state of polarization (SoP) can be indicated by (SoP) $|n\rangle$.

First, assume that the incident wave is linearly polarized (SoP) $|LP\rangle$ and the electric field can be expressed as Eq. (4):

$$\vec{E}_i = \left(E_{ix}\hat{x} + E_{iy}e^{i\delta}\hat{y}\right)e^{i\vec{k_0}\vec{r}} \tag{4}$$

where $\delta = 0$, which is the phase difference between the x- and y-components of the incident electric field. E_{ix} and E_{iy} are the amplitudes of the x- and y-components of the incident electric field, respectively. $E_{iy}/E_{ix} = \tan\alpha$, where α is the angle between the polarization direction of the incident wave and the x-direction. The electric field of the transmitted wave can be expressed as Eq. (5):

$$\vec{E}_t = \left(T_{x-LP}\hat{x} + T_{y-LP}\hat{y}\right)e^{i\vec{k_0}\vec{r}} \tag{5}$$

The coefficients of the transmitted EM wave along the x- and y-polarized can be expressed as $T_{x-LP} = t_{x-LP}e^{i\varphi_{x-LP}}$ and $T_{y-LP} = t_{y-LP}e^{i\varphi_{y-LP}}$, where t_{x-LP} and t_{y-LP} are the amplitudes of transmission coefficients T_{x-LP} and T_{y-LP}, besides φ_{x-LP} and φ_{y-LP} are the phases. When $\alpha = 45°$, which corresponds to $E_{iy}/E_{ix} = 1$, the simulated results of x- and y-polarized transmission coefficients when the PIN diodes are in different states are demonstrated in Figs. 4c-d. It's worth noting that because the metasurface has no effect on x-polarized waves, t_{x-LP} is constant and equal to 0.707. In addition, the y-polarized transmission amplitudes are around 0.65 in the frequency range of 9.4-11.8 GHz, which are almost equal to the x-polarized. Fig. 4e illustrates the proportionality of t_{x-LP} and t_{y-LP}, enabling a visual comparison of the magnitudes of the x- and y-polarized. By changing the states of the PIN diodes, the phase of the y-polarized transmitted wave can be dynamically shifted from 0° to 360°, leading to the phase difference between the x- and y-polarized transmitted wave $\Delta\varphi$ covering 360°, as shown in Fig. 4f.

To study polarization states of transmitted waves, four Stokes parameters are introduced as the following Eq. (6):

$$\begin{cases} I = \left|t_{y-LP}\right|^2 + \left|t_{x-LP}\right|^2 \\ Q = \left|t_{x-LP}\right|^2 - \left|t_{y-LP}\right|^2 \\ U = 2\left|t_{y-LP}\right|\left|t_{x-LP}\right|\cos\Delta\varphi \\ V = 2\left|t_{y-LP}\right|\left|t_{x-LP}\right|\sin\Delta\varphi \end{cases} \tag{6}$$

and the ellipticity angle χ and orientation angle ψ can be obtained from Eqs. (7) and (8):

$$\sin 2\chi = \frac{V}{I} \tag{7}$$

$$\tan 2\psi = \frac{U}{Q} \tag{8}$$

Theoretically, t_{x-LP} and t_{y-LP} are nearly equal, and $\Delta\varphi$ covers 360° so that an arbitrary ellipticity angle χ can be achieved. As shown in Fig. 5a, when the state of PIN diodes is in S5, the calculated χ exceeds 33° in a frequency band of 11.0-11.9 GHz. In this case, the LP wave is converted to the left-handed circularly polarized (LCP). Furthermore, Fig. 5c shows that the calculated χ is lower than -33° in a frequency band of 9.0-9.6 GHz when the state of PIN diodes is in S9. The LP wave is converted to the right-handed circularly polarized (RCP). As shown in Fig. 5b, when the state of PIN diodes is in S7, the

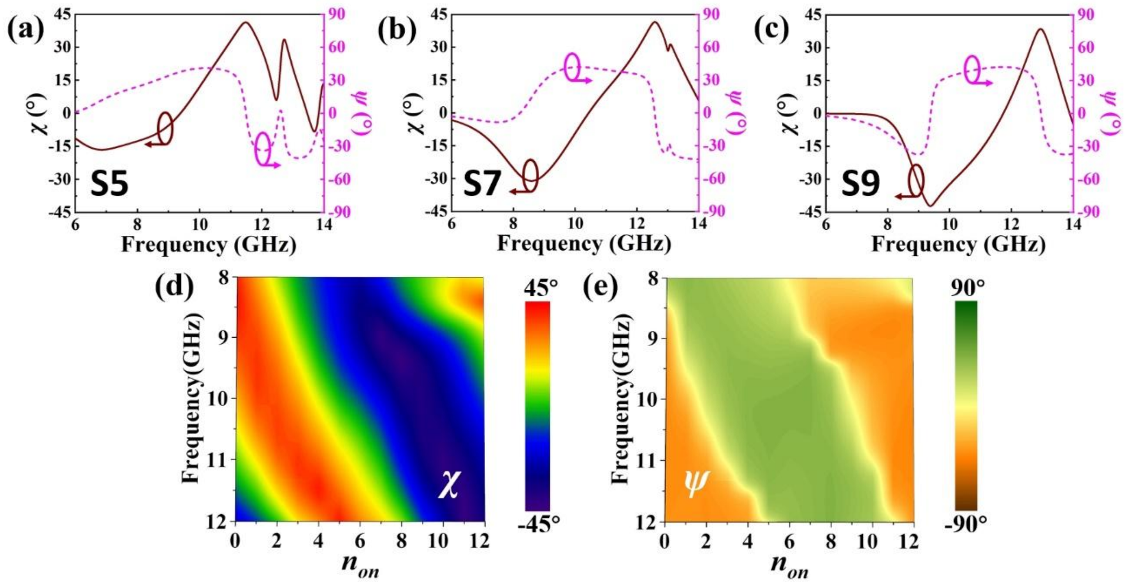

Fig. 5: a-c) The calculated ellipticity angle χ and orientation angle ψ when the state of PIN diodes is in S5, S7, and S9, respectively. d) The results of the calculated ellipticity angle χ in different states of PIN diodes. e) The results of the calculated orientation angle ψ in different states of PIN diodes.

calculated χ is within -5° to 5° in a frequency band of 10.2-10.7 GHz and even approaches 0° at 10.4 GHz. In this case, the LP wave is converted to another linear polarization. In addition, the results of the ellipticity angle χ and orientation angle ψ in other states are shown in Figs. 5d-e.

In fact, when α = 45°, the y-polarized transmission amplitudes can only be considered approximately equal to the x-polarized due to the losses incurred in the y-direction; however, they are never precisely equivalent. This discrepancy results in the ellipticity angle χ failing to precisely reach 45°, and also low efficiency in circular polarization conversion. Therefore, the incident polarization angle α is corrected, and y-polarized transmission amplitudes are increased to compensate for the loss. When α = 49°, which corresponds to E_{iy}/E_{ix} = 1.15, the simulated results of x- and y-polarized transmission coefficients when the PIN diodes are in different states are demonstrated in Figs. 6a-b. In this case, the x-polarized transmission amplitudes are constant and equal to 0.66 and the y-polarized transmission amplitudes are around 0.66 in the frequency range of 9.4-11.8 GHz, which are almost equal to the x-polarized, as shown in Fig. 6c. After the correction of the incident polarization angle α, the efficiency of polarization modulation of the proposed active metasurface is enhanced, as shown in Figs. 6d-f. When the state of PIN diodes is in S5, the calculated χ exceeds 33° in a frequency band of 11.0-11.9 GHz and even reaches 44.6° at 11.5 GHz. In this case, the LP wave is converted to the LCP. Furthermore, the calculated χ is lower than -33° in a frequency band of 9.0-10.0 GHz and even reaches -43.8° at 9.4 GHz when the state of PIN diodes is in S9. The LP wave is converted to the RCP. When the state of PIN diodes is in S7, calculated χ is within -5° to 5° in a frequency band of 10.2-10.7 GHz and even approaches 0° at 10.4 GHz. In this case, the LP wave is converted to another linear polarization. In addition, the results of corrected ellipticity angle χ and orientation angle ψ in other states are shown in Figs. 6g-h.

Polarization modulation realized by the proposed metasurface shows the characteristic of wide frequency dispersion. For each state, the polarization state of the transmitted wave varies with the change of frequency. For example, when the PIN diodes are in S8 (n_{on}= 7), the calculated χ is about -45° at 9.0 GHz, and the transmitted wave is the RCP. As the frequency increases, the calculated χ increases, and the transmitted wave becomes an elliptically polarized wave. When it reaches 11.0 GHz, the elliptical angle reaches 0, and the polarization state turns to (SoP) $\left|LP\right\rangle$. Moreover, by changing the state of the PIN diodes, the polarization state of the transmitted wave can be manipulated dynamically at the same frequency. At 12.0 GHz, as shown in Fig. 7a, the calculated χ increases from -22° to +45° and then decreases from +45° to -45°, and finally increases to -33° as n_{on} increases and the polarization state of the transmitted wave goes through the following stages. First, it changes from right elliptical polarization to line polarization, then to left circular polarization wave, then to line polarization wave, then to right circular polarization wave, and finally to right elliptical polarization. Similar dynamic modulation capabilities for polarization states of the transmitted wave are demonstrated at other frequencies. As shown in Fig. 7b, the orientation angle ψ both are about 40° until n_{on} is less than 5, then drops sharply to approximately -40°, and then remains essentially unchanged, indicating that the orientation angle of the polarization state is relatively stable at 9.0 GHz. In addition, similar characteristics for the stable orientation angle can also be found in other frequencies.

Then, assume that the incident wave is circularly polarized

(SoP) $\left|CP\right\rangle$ and the electric field can be expressed as Eq. (9):

$$\vec{E}_i = \left(E_{ix}\hat{x} + E_{iy}e^{i\delta}\hat{y} \right) e^{i\overrightarrow{k_0}\vec{r}} \tag{9}$$

where $\delta = \pm\pi/2$ ("+" and "-" are related to LCP and RCP, respectively) and $E_{iy}/E_{ix} = 1$. The electric field of the transmitted wave can be expressed as Eq. (10):

$$\vec{E}_t = \left(T_{x-CP}\hat{x} + T_{y-CP}\hat{y} \right) e^{i\overrightarrow{k_0}\vec{r}} \tag{10}$$

The coefficients of the transmitted EM wave along the x- and y-polarized can be expressed as $T_{x-CP} = t_{x-CP}e^{i\varphi_{x-CP}}$ and $T_{y-CP} = t_{y-CP}e^{i\varphi_{y-CP}}$, where t_{x-CP} and t_{y-CP} are the amplitudes of transmission coefficients T_{x-CP} and T_{y-CP}, besides φ_{x-CP} and φ_{y-CP} are the phases.

Similarly, dynamic modulation of the polarization states can be achieved by changing the states of the PIN diodes. To achieve circularly polarized dynamic conversion and the implementation of the spin-to-orbital angular momentum converter, we have selected two states S1, S7, and S13 of the diodes as a demonstration. Figs. 8a-c show the normalized

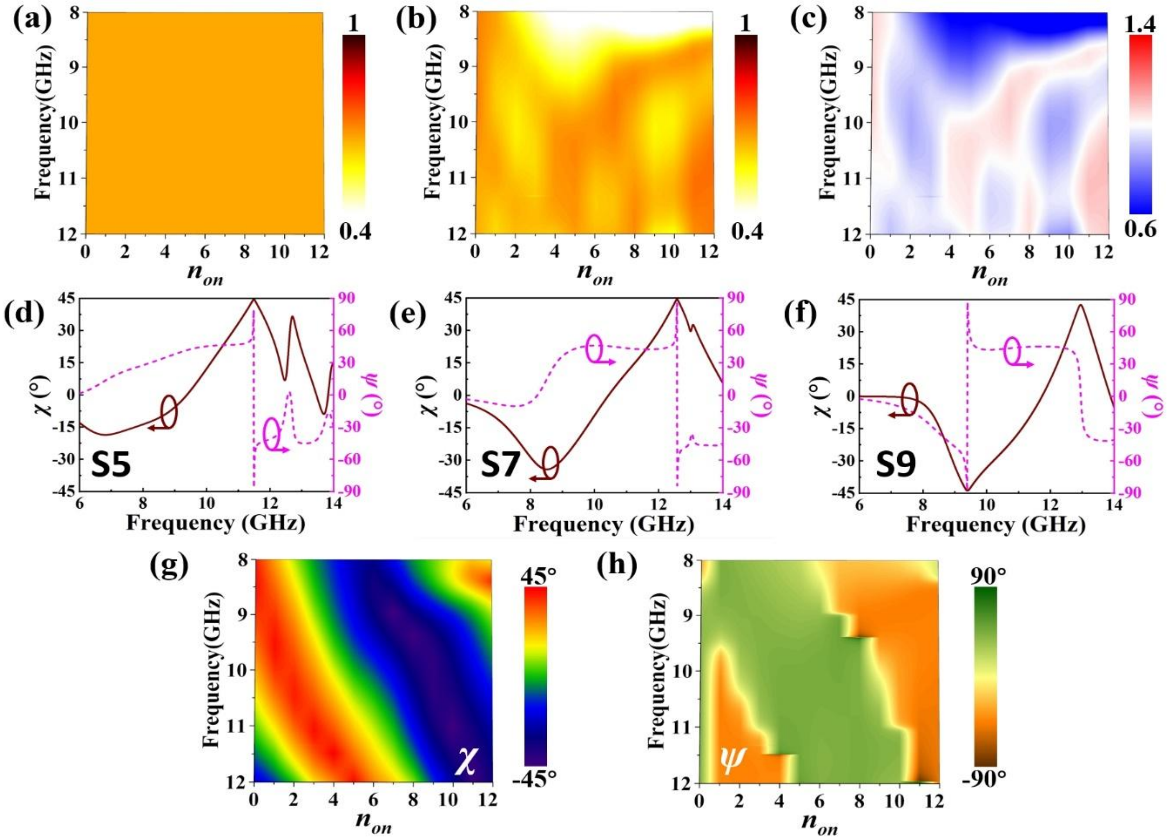

Fig. 6: a-b) The x- and y-polarized transmission amplitude in different states of PIN diodes after correction for the incident polarization angle, respectively. d-f) The corrected ellipticity angle χ and orientation angle ψ when the state of PIN diodes is in S5, S7, and S9, respectively. g) The results of the corrected ellipticity angle χ in different states of PIN diodes. h) The results of the corrected orientation angle ψ in different states of PIN diodes.

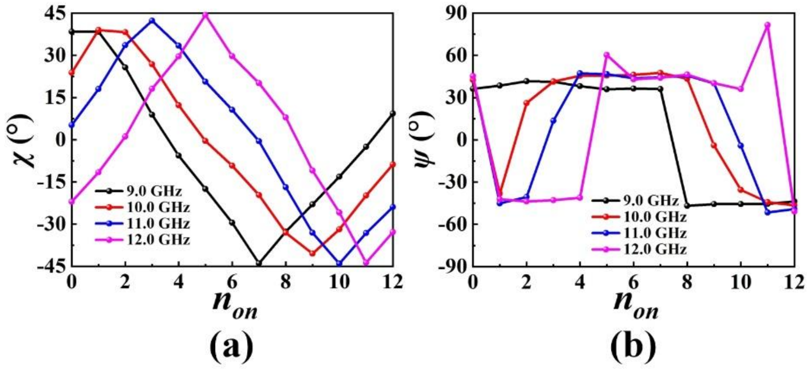

Fig. 7: a-b) At 9, 10, 11, and 12 GHz, calculated ellipticity angle χ and orientation angle ψ with the different number of PIN diodes in the "on" state, respectively.

cross-polarization amplitudes under (SoP) $\left|LCP\right\rangle$ and (SoP) $\left|RCP\right\rangle$, respectively. In S1 and S13, the cross-polarization amplitudes exceed 0.9 in 10.1-11.8 GHz and 8.8-11.0 GHz, respectively. Therefore, the circularly polarized incident waves can be converted into the cross-polarized transmitted waves in these two states by the designed meta-atom. At this time, the phase difference is governed by PB phases ($\Delta\varphi = \pm 2\gamma$, where "+" and "−" are for LCP and RCP, γ is the rotation angle). Based on the proposed meta-atoms, can be generated. However, the cross-polarized amplitudes are below 0.2, and co-polarized amplitudes exceed 0.9 in 9.9-11.0 GHz when the PIN diodes are in S7. The circular polarization state remains unchanged, and there is no polarization conversion.

3. Results and discussion

As a proof-of-concept, a spin-to-orbital angular momentum dynamic converter with quasi-continuous spatial phase response based on the PB phase generated by the circular polarization conversion is implemented. It has been known that an electromagnetic vortex is closely related to an azimuthal phase dependence $\exp(il\theta)$, which carries an orbital angular momentum equivalent to $l\hbar$ ($\hbar$ is the reduced Planck constant), where θ is the angle between the corresponding curvature radius and the vertical direction.[16] The integer topological charge l corresponds to the number of wavefront helices within a single wavelength. Consequently, generating such a vortex beam requires imparting a helical phase front with a $2\pi l$ azimuthal variation. The traditional metasurface-based method arranges unit cells in discrete sectors. In order to generate a rotated phase distribution, the unit cells in different sectors are non-identical. To avoid the phase deviations typically encountered at sector boundaries in discretely segmented metasurfaces, our proposed strategy aligns meta-atoms along an Archimedean spiral, which enables the structural integrity of the spin–orbital converter while keeping periodic boundary conditions between each element, and improves mode purity and efficiency in spin-to-orbital angular momentum conversion. As shown in Fig. 8d, the meta-atoms are aligned along the Archimedes spiral, and the tangent direction of each point on the curve can be considered to approximately satisfy the PB phase. In this way, the rotated phase gradients with "quasi-continuous distribution" can be obtained. The mathematical expression of Archimedean spiral in polar coordinates can be expressed as: $r(\gamma) = a_0 + b_0\gamma$, where a_0 =10mm and denotes the distance from the starting point to the coordinate origin, b_0 = g/2π and is fixed to 2.86 mm, which represents the increment with the increase of spiral angle and is matched with the distance between the dielectrics g of the proposed meta-atom. It's known that if the curve is circular or quasi-circular, the angular difference can cover 0°-360° when starting from any point on the curve around the circle. Accordingly, the phase changes quasi-continuously over a range of 0°-720°. The topological charge can be expressed as $l = d\varphi/d\theta = \pm 2d\gamma/d\theta = \pm 2$. Therefore, when the diodes are in S1 and S13, the transmitted wave will be converted into a vortex beam carrying OAM with $l = \pm 2$ under the circularly polarized wave incidence.

For validation, a spin-to-orbital angular momentum converter with a diameter of 240 mm is constructed as illustrated in Fig. 8e. The near-field performance of the designed model is simulated by CST, and the simulated E_y-component electric field distributions are shown in Figs. 9a-f. The cut plane is selected to be parallel to the xoy-plane with a

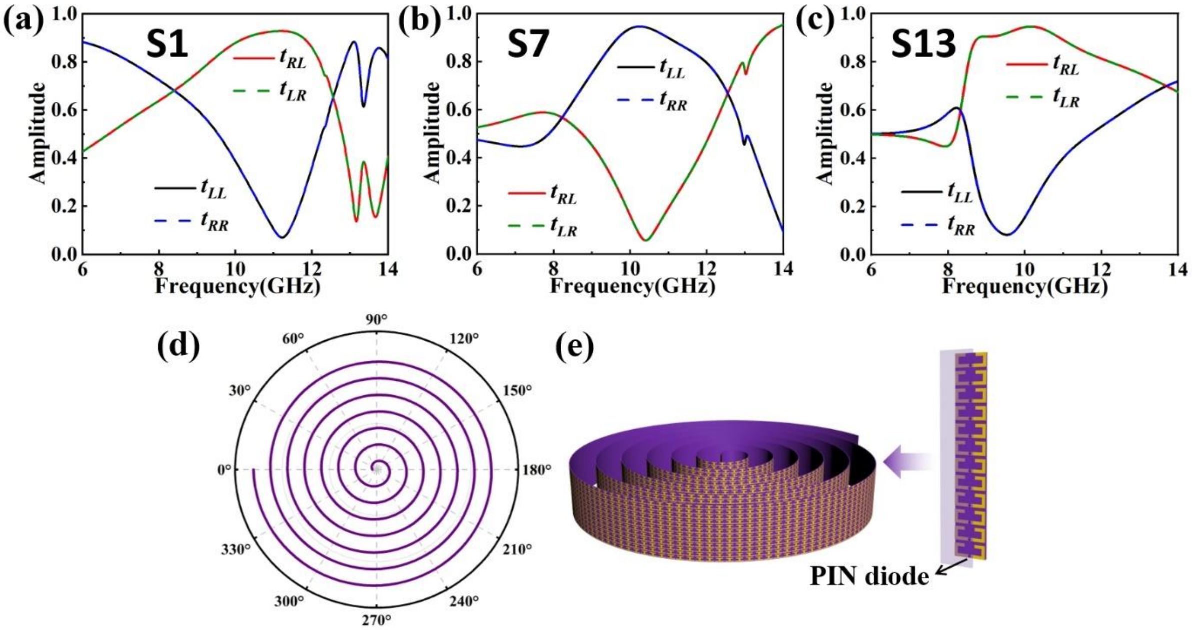

Fig. 8: a-c) Cross-polarization curves under both normal left- and right-handed circularly polarized waves in S1, S7, and S13, respectively. d)The conceptual helix curve of the proposed spin-to-orbital angular momentum converter. e) The topology of the model of the proposed spin-to-orbital angular momentum converter and the meta-atom.

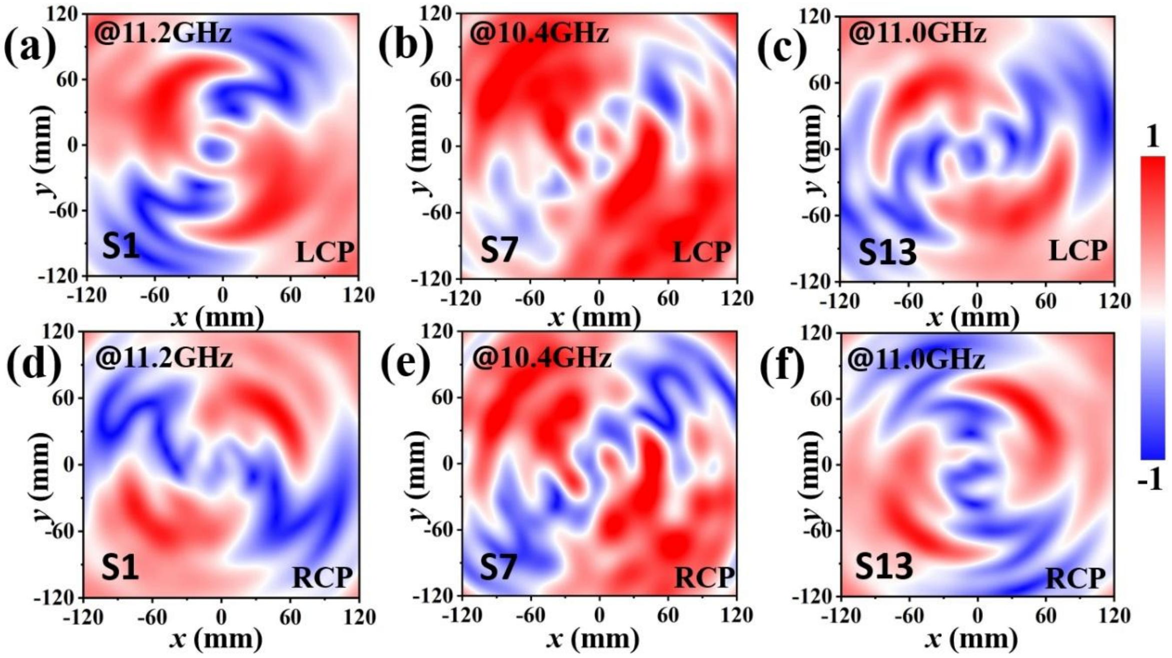

Fig. 9: Simulated E_y-component of the electric field distributions at the cutting plane, which is parallel to the *xoy*-plane with a distance of 100 mm. a) and d) The electric field distributions when the PIN diodes are in S1 under the incidence of LCP and RCP waves at 11.2 GHz, respectively. b) and e) The electric field distributions when the PIN diodes are in S7 under the incidence of LCP and RCP waves at 10.4 GHz, respectively. c) and f) The electric field distributions when the PIN diodes are in S13 under the incidence of LCP and RCP waves at 11.0 GHz, respectively.

distance of 100 mm. For the simulation settings, the Open add space is applied as the boundary condition in all directions. The port is set as the circular polarization basis, and the Time Domain Solver is set for the simulation. Figs. 9a and 9d demonstrate the electric field distributions under the LCP and RCP waves at 11.2 GHz when the PIN diodes are in S1. In addition, the maps under the LCP and RCP waves at 11.0 GHz with the PIN diodes in S13 are depicted in Figs. 9c and 9f. The simulated electric field distributions clearly show the characteristic semi-circular yin-yang fish-shaped intensity profiles with central nulls, and the number of intensity lobes in the azimuthal direction further validates the charge value. It can be observed that the vortex beams with a topological charge number of $l = \pm 2$ are generated. When the PIN diodes are in S7, the maps under the LCP and RCP waves at 10.4 GHz are depicted in Figs. 9b and 9e. There is no vortex beam with the topological charge number. And dynamic customization of the topological charge number will be achieved. In addition, vortex beams with other topological charges can be obtained by rearrangement of the meta-atoms.

To verify the feasibility of our design, the prototype is fabricated by low-cost printed circuit board (PCB) technology, and the measurement is carried out in a microwave anechoic chamber as shown in Fig. 10. In order to bend the metasurface along the given Archimedean spiral, the prototype is fixed in a polymethacrylimide (PMI) rigid foam with a dielectric constant of 1.06, which has a negligible effect on the results. To simplify the drive circuit, a series bias network is implemented to reduce the number of control lines to 12. The near-field property of the prototype is tested by the near-field scanning technique. The prototype is placed between the probe and the circularly polarized horn antenna, and the probe is 100 mm away from the prototype. When all PIN diodes are inactivated (S1), the electric field distributions of the E_y-component at 11.2 GHz under the incidence of LCP and RCP waves are shown in Figs. 11a and 11d. Figs. 11c and11f show the maps at the frequency points of 11.0 GHz under the incidence of LCP and RCP waves when all PIN diodes are activated (S13). The measured results show that a topological charge number of $l = \pm 2$ is obtained when the PIN diodes are in those two states, which are in general agreement with the simulation results and prove the feasibility of the proposed method. However, when PIN diodes are in S7, there is no vortex beam with the topological charge number, as illustrated in Figs. 11b and 11e. Due to the processing tolerances or the fact that the incident wave source is not strictly planar, the intensity of the measured electric field distribution differs slightly from the simulated results. The experimental results show that the metasurface demonstrates excellent stability under various room-temperature conditions. Its power consumption is effectively managed during dynamic operation, resulting in favorable overall energy efficiency. The system shows strong potential for practical applications, with opportunities for further energy-saving improvements in future iterations.

To evaluate the performance of the novel design, Table 1 lists a comparison of this effort with previous works. It can be observed that our design for dynamic modulation of

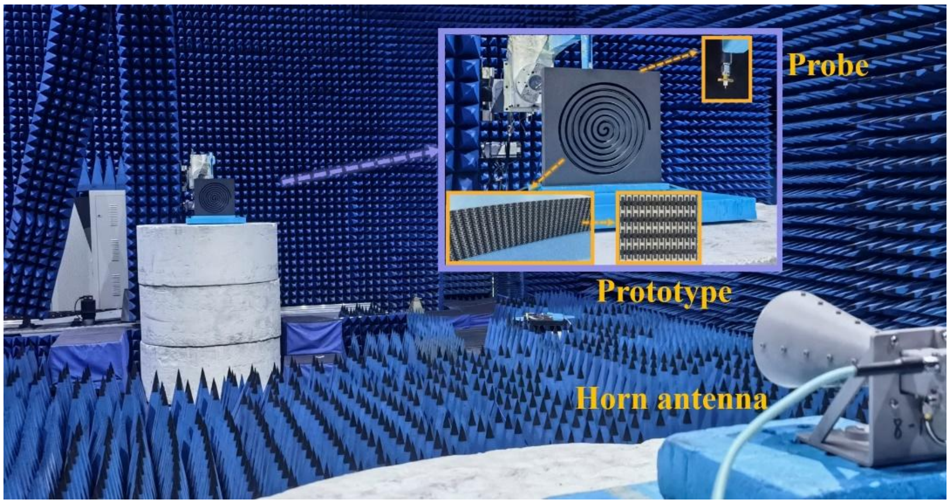

Fig. 10: The experimental setup for near-field scanning with the fabricated prototypes.

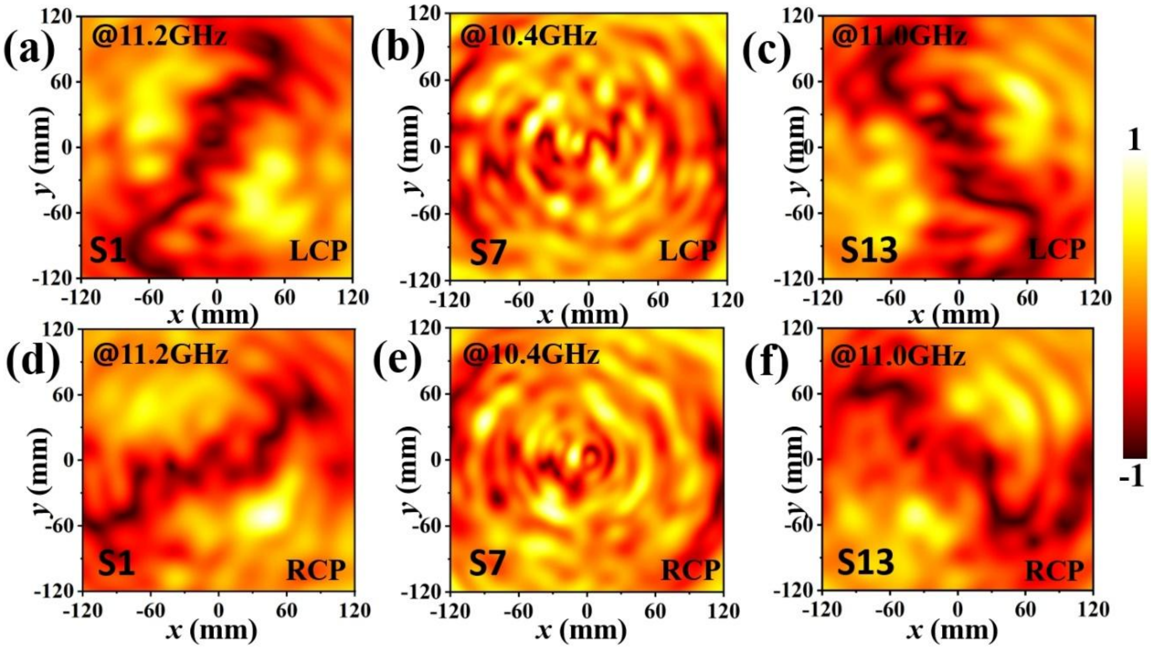

Fig. 11: Measured E_y-component of the electric field distributions at the cutting plane, which is parallel to the *xoy*-plane with a distance of 100 mm. a) and d) The electric field distributions when the PIN diodes are in S1 under the incidence of LCP and RCP waves at 11.2 GHz, respectively. b) and e) The electric field distributions when the PIN diodes are in S7 under the incidence of LCP and RCP waves at 10.4 GHz, respectively. c) and f) The electric field distributions when the PIN diodes are in S13 under the incidence of LCP and RCP waves at 11.0 GHz, respectively.

Table 1: Comparison between our work and other designs.

Ref./Year	Bandwidth [GHz]	Number of states	Transmission efficiency	Transmission/reflection
[27]/2016	13.7-14.9 GHz	2	-1 dB	transmission
[28]/2020	4.7-5.9 GHz	2	-1 dB	transmission and reflection
[29]/2021	2.77 GHz	4	−3.65 dB	transmission
[39]/2023	2.5-3.5 GHz	4	-3 dB	transmission
[40]/2023	3.03-3.6 GHz	2	-2 dB	transmission
[42]/2023	2.5-3.64 GHz	2	−3 dB	transmission
This work	8.8-11.8 GHz	13	-1 dB	transmission

transmissive polarization states has properties in both broadband frequency and a wide scope of regulation compared to others. Therefore, our work provides an alternative way to dynamically modulate the transmission polarization state and has promising applications in polarized antennas.

4. Conclusion

In summary, a strategy to dynamically control the polarization state in real-time and achieve efficient transmission by tailoring the transmission phase is proposed. Controlling the state of the voltage-driven PIN diodes enables the switching of the transmission mode between the waveguide and the SSPP. The proposed strategy achieves efficient dynamic tunable functions in transmission and diverse polarization states with the characteristic of wide frequency dispersion and powerful controllability. And it will provide a new platform for versatile transmission-type-based EM devices. As verification, a spin-to-orbital angular momentum dynamic converter based on the PB phase generated by the circular polarization conversion is demonstrated. The experimental and simulation results are in agreement, proving the feasibility of the proposed strategy. Moreover, the re-arrangement of the meta-atoms will enable vortex beams with other topological charges. By extension to time-varying modulation, dynamic customization of the topological charge number will be achieved. The proposed approach enables an alternative architecture for modulating polarization, which has great envisions for future wireless communication and detection systems.

Acknowledgments

This work is sponsored by the National Key Research and Development Program of China (Grant Nos. 2022YFB3806200), the National Natural Science Foundation of China (Grant Nos. 52272101), and the Natural Science Foundation of Shaanxi Province (Grant Nos. 2020JM-342).

Conflict of Interest

There is no conflict of interest.

Supporting Information

Not applicable.

CRediT Statement

Zhe Qin: Writing – Original draft, Supervision, Resources, Investigation, Formal analysis. **Yongfeng Li**: Writing – review & editing, Supervision, Resources, Project administration, Investigation, Funding acquisition. **He Wang**: Writing – review & editing, Supervision. **Zhibiao Zhu**: Methodology, Investigation, Formal analysis. **Lixin Jiang**: Investigation, Formal analysis, Data curation. **Wanwan Yang**: Investigation, Formal analysis, Data curation. **Hongya Chen**: Supervision, Resources. **Lin Zheng**: Supervision, Resources, Project administration. **Jiafu Wang**: Supervision, Resources, Project administration. **Hua Ma**: Supervision, Resources.

References

[1] R. A. Shelby, D. R. Smith, S. Schultz, Experimental verification of a negative index of refraction, *Science*, 2001, **292**, 77-79, doi: 10.1126/science.1058847.

[2] S. Zhang, Y. S. Park, J. Li, X. Lu, W. Zhang, X. Zhang, Negative refractive index in chiral metamaterials, *Physical Review Letters*, 2009, **102**, 023901, doi: 10.1103/physrevlett.102.023901.

[3] N. Yu, P. Genevet, M. A. Kats, F. Aieta, J. P. Tetienne, F. Capasso, Z. Gaburro, Light propagation with phase discontinuities: generalized laws of reflection and refraction, *Science*, 2011, **334**, 333-337, doi: 10.1126/science.1210713.

[4] D. R. Smith, S. Schultz, P. Markoš, C. M. Soukoulis, Determination of effective permittivity and permeability of metamaterials from reflection and transmission coefficients, *Physical Review B*, 2002, **65**, 195104, doi: 10.1103/physrevb.65.195104.

[5] L. Jiang, Y. Li, H. Yang, M. Yan, J. Jiang, Y. Zhang, Z. Qin, W. Yang, H. Chen, Y. Pang, Z. Guo, L. Zheng, J. Wang, S. Qu, Beam scanning with ultra-low sidelobes and in-band ultra-low scattering characteristics empowered by single space-time-coding radiation-scattering metasurface, *Advanced Science*, 2025, **12**, e2413429, doi: 10.1002/advs.202413429.

[6] D. Schurig, J. J. Mock, B. J. Justice, S. A. Cummer, J. B. Pendry, A. F. Starr, D. R. Smith, Metamaterial electromagnetic cloak at microwave frequencies, *Science*, 2006, **314**, 977-980, doi: 10.1126/science.1133628.

[7] H. Chu, Q. Li, B. Liu, J. Luo, S. Sun, Z. Hang, L. Zhou, Y. Lai, A hybrid invisibility cloak based on integration of transparent metasurfaces and zero-index materials, *Light: Science & Applications*, 2018, **7**, 50, doi: 10.1038/s41377-018-0052-7.

[8] X. Ni, Z. J. Wong, M. Mrejen, Y. Wang, X. Zhang, An ultrathin invisibility skin cloak for visible light, *Science*, 2015, **349**, 1310-1314, doi: 10.1126/science.aac9411.

[9] Z. Qin, C. Li, M. Yan, Y. Li, H. Wang, J. Wang, H. Ma, Polarization- and angle-insensitive frequency-tunable metasurface absorber with multi-tailoring modes, *Optics Express*, 2025, **33**, 26565-26577, doi: 10.1364/OE.554230.

[10] Y. Cheng, Y. Li, H. Wang, H. Chen, W. Wan, J. Wang, L. Zheng, J. Zhang, S. Qu, Ohmic dissipation-assisted complex amplitude hologram with high quality, *Advanced Optical Materials*, 2021, **9**, 2002242, doi: 10.1002/adom.202002242.

[11] H. Wang, Z. Qin, L. Huang, Y. Li, R. Zhao, H. Zhou, H. He, J. Zhang, S. Qu, Metasurface with dynamic chiral meta-atoms for spin multiplexing hologram and low observable reflection, *PhotoniX*, 2022, **3**, 10, doi: 10.1186/s43074-022-00057-1.

[12] L. Li, T. Cui, W. Ji, S. Liu, J. Ding, X. Wan, Y. Li, M. Jiang, C. Qiu, S. Zhang, Electromagnetic reprogrammable coding-metasurface holograms, *Nature Communications*, 2017, **8**, 197, doi: 10.1038/s41467-017-00164-9.

[13] G. Biener, A. Niv, V. Kleiner, E. Hasman, Formation of

helical beams by use of Pancharatnam–Berry phase optical elements, *Optics Letters*, 2002, **27**, 1875-1877, doi.org: 10.1364/OL.27.001875.

[14] E. Nagali, F. Sciarrino, F. De Martini, L. Marrucci, B. Piccirillo, E. Karimi, E. Santamato, Quantum information transfer from spin to orbital angular momentum of photons, *Physical Review Letters*, 2009, **103**, 013601, doi: 10.1103/PhysRevLett.103.013601.

[15] L. Yang, S. Sun, W. E. I. Sha, Manipulation of orbital angular momentum spectrum using shape-tailored metasurfaces, *Advanced Optical Materials*, 2021, **9**, 2001711, doi: 10.1002/adom.202001711.

[16] H. Wang, Y. Li, H. Chen, Y. Shen, Z. Yang, J. Wang, J. Zhang, M. Ding, A. Zhang, T. Cui, S. Qu, Spin-to-orbital angular momentum conversion with quasi-continuous spatial phase response, *Advanced Optical Materials*, 2019, **7**, 1901188, doi: 10.1002/adom.201901188.

[17] G. Wu, K. Chan, K. Shum, C. Chan, Millimeter-wave holographic flat lens antenna for orbital angular momentum multiplexing, *IEEE Transactions on Antennas and Propagation*, 2021, **69**, 4289-4303, doi: 10.1109/TAP.2020.3048527.

[18] Y. Li, J. Zhang, S. Qu, J. Wang, L. Zheng, Y. Pang, Z. Xu, A. Zhang, Achieving wide-band linear-to-circular polarization conversion using ultra-thin bi-layered metasurfaces, *Journal of Applied Physics*, 2015, **117**, 044501, doi: 10.1063/1.4906220.

[19] Y. Cheng, C. Fang, X. S. Mao, R. Z. Gong, L. Wu, Design of an ultrabroadband and high-efficiency reflective linear polarization convertor at optical frequency, *IEEE Photonics Journal*, 2016, **8**, 7805509, doi: 10.1109/JPHOT.2016.2624559.

[20] Y. Cheng, Y. Nie, Z. Cheng, L. Wu, X. Wang, R. Z. Gong, Broadband transparent metamaterial linear polarization transformer based on triple-split-ring resonators, *Journal of Electromagnetic Waves and Applications*, 2013, **27**, 1850-1858, doi: 10.1080/09205071.2013.825891.

[21] E. Doumanis, G. Goussetis, J. L. Gomez-Tornero, R. Cahill, V. Fusco, Anisotropic impedance surfaces for linear to circular polarization conversion, *IEEE Transactions on Antennas and Propagation*, 2012, **60**, 212-219, doi: 10.1109/TAP.2011.2167920.

[22] Y. Li, Y. Pang, J. Wang, Q. Zheng, M. Feng, H. Ma, J. Zhang, Z. Xu, S. Qu, Wideband polarization conversion with the synergy of waveguide and spoof surface plasmon polariton modes, *Physical Review Applied*, 2018, **10**, 064002, doi: 10.1103/physrevapplied.10.064002.

[23] M. Euler, V. Fusco, R. Dickie, R. Cahill, J. Verheggen, Sub-mm wet etched linear to circular polarization FSS based polarization converters, *IEEE Transactions on Antennas and Propagation*, 2011, **59**, 3103-3106, doi: 10.1109/TAP.2011.2158973.

[24] M. G. Silveirinha, Design of linear-to-circular polarization transformers made of long densely packed metallic helices, *IEEE Transactions on Antennas and Propagation*, 2008, **56**, 390-401, doi: 10.1109/TAP.2007.915428.

[25] X. Wu, Y. Meng, L. Wang, J. Tian, S. Dai, W. Wen, Anisotropic metasurface with near-unity circular polarization conversion, *Applied Physics Letters*, 2016, **108**, 183502, doi: 10.1063/1.4948594.

[26] X. Huang, J. Chen, H. Yang, High-efficiency wideband reflection polarization conversion metasurface for circularly polarized waves, *Journal of Applied Physics*, 2017, **122**, 043102, doi: 10.1063/1.4996643.

[27] Z. Qin, Y. Li, H. Wang, W. Wan, C. Li, Z. Zhu, Y. Cheng, S. Li, H. Chen, J. Wang, S. Qu, Polarization meta-converter for dynamic polarization states shifting with broadband characteristic, *Optics Express*, 2022, **30**, 20014-20025, doi: 10.1364/OE.453691.

[28] W. Li, S. Xia, B. He, J. Chen, H. Shi, A. Zhang, Z. Li, Z. Xu, A reconfigurable polarization converter using active metasurface and its application in horn antenna, *IEEE Transactions on Antennas and Propagation*, 2016, **64**, 5281-5290, doi: 10.1109/TAP.2016.2620484.

[29] L. Chen, Q. Ma, Q. F. Nie, Q. R. Hong, H. Y. Cui, Y. Ruan, T. J. Cui, Dual-polarization programmable metasurface modulator for near-field information encoding and transmission, *Photonics Research*, 2021, **9**, 116-124, doi.org: 10.1364/PRJ.412052.

[30] Y. Bai, C. Ouyang, S. Zhang, Z. Yao, K. Liu, S. Liu, J. Ma, Y. Li, T. Cao, Z. Tian, $Ge_2Sb_2Te_5$-based efficient switching between a cross-polarization conversion and a circular-to-linear polarization conversion, *Optics Letters*, 2023, **48**, 5843-5846.

[31] S. Zhang, X. Chen, K. Liu, H. Li, Y. Xu, X. Jiang, Y. Xu, Q. Wang, T. Cao, Z. Tian, Nonvolatile reconfigurable dynamic Janus metasurfaces in the terahertz regime, *Photonics Research*, 2022, **10**, 1731, doi: 10.1364/prj.456161.

[32] S. K. Ghosh, S. Das, S. Bhattacharyya, Transmittive-type triple-band linear to circular polarization conversion in THz region using graphene-based metasurface, *Optics Communications*, 2021, **480**, 126480, doi: 10.1016/j.optcom.2020.126480.

[33] H. Zhang, B. Wei, J. Dong, Q. Zang, C. Huang, X. Bai, L. Tang, H. Shi, C. Liu, Y. Liu, Y. Lu, Tunable broadband transmissive terahertz cross-polarization converter enabled by a hybrid metal-graphene metasurface, *Results in Physics*, 2023, **44**, 106190, doi: 10.1016/j.rinp.2022.106190.

[34] Z. Wang, L. Jing, K. Yao, Y. Yang, B. Zheng, C. M. Soukoulis, H. Chen, Y. Liu, Origami-based reconfigurable metamaterials for tunable chirality, *Advanced Materials*, 2017, **29**, 1700412, doi: 10.1002/adma.201700412.

[35] Z. Zhu, Y. Li, J. Wang, L. Jiang, Z. Qin, L. Zheng, H. Chen, W. Wang, S. Qu, Miura origami-inspired reconfigurable phase gradient metasurface for linearly and circularly polarized differential modulation, *Advanced Photonics Research*, 2024, **5**, 2400025, doi: 10.1002/adpr.202400025.

[36] X. Ma, W. Pan, C. Huang, M. Pu, Y. Wang, B. Zhao, J. Cui, C. Wang, X. Luo, An active metamaterial for polarization manipulating, *Advanced Optical Materials*, 2014, **2**, 945-949, doi: 10.1002/adom.201400212.

[37] Z. Wu, Y. Ra'di, A. Grbic, Tunable metasurfaces: a polarization rotator design, *Physical Review X*, 2019, **9**, 011036, doi: 10.1103/physrevx.9.011036.

[38] P. Wang, F. Lin, Y. Wang, H. Zhou, Z. Yan, J. Gao, J. Ye, J. Ai, Tunable polarization converter with high polarization isolation based on metasurface and its application on horn antenna, *Applied Physics A*, 2022, **128**, 863, doi: 10.1007/s00339-022-05930-1.
[39] H. Zhou, X. Yu, P. Wang, Y. Wang, Z. Yan, Wideband linear-to-multi-polarization converter based on active metasurface, *IEEE Transactions on Antennas and Propagation*, 2023, **71**, 5246-5255, doi: 10.1109/TAP.2023.3256581.
[40] P. Wang, Y. Qin, Y. Wang, H. Zhou, Z. Yan, Wideband switchable linear polarization rotator based on metasurface, *Applied Physics Letters*, 2023, **123**, 011701, doi: 10.1063/5.0155015.
[41] NXP Semiconductors, planar PIN diode in a SOD523 ultrasmall SMD plastic package, BAP70-02.
[42] S. S. Zhu, P. Wang, Y. Zhang, Z. M. Yan, Y. Wang, H. C. Zhou, A reconfigurable polarization converter and related application as horn antenna cladding, *Journal of Applied Physics*, 2023, **133**, 023102, doi: 10.1063/5.0130212.

Open Access